erage burial depth than that of any of the samples measured by these authors. Using a ratio of 1.6 should provide a conservative value for the cosmic ray–induced ^{129}Xe component. The nucleon lifetime limit thus obtained is 1.6×10^{25} years (*19*). This is probably an underestimate since it is possible that all of the observed excess ^{129}Xe is produced by cosmic rays. The observed ratio of 2.5 seems, if anything, unexpectedly low.

The nucleon lifetime limit obtained in this work represents an improvement by about two orders of magnitude over the previous (*9*) rigorous limit on nucleon stability. Some further improvement could probably be obtained if a sample with greater average burial depth were available. Uncertainties in background effects, however, would probably prevent any very large improvement.

Alternative approaches to this problem have been described (*20, 21*) in which very large samples with favorable radiochemical properties are used to search with high sensitivity for a small number of nucleon decay–produced radioactive atoms. Such methods are capable of measuring nucleon lifetimes greater than 10^{28} years. In addition, background effects (other than those due to neutrino interactions) could be controlled through burial depth, local shielding, and sample prepurification.

JOHN C. EVANS, JR.*
Chemistry Department, Brookhaven National Laboratory, Upton, New York 11973

RICHARD I. STEINBERG
Physics Department, University of Pennsylvania, Philadelphia 19104

References and Notes

1. E. C. G. Stückelberg, *Helv. Phys. Acta* **11**, 317 (1938).
2. E. P. Wigner, *Proc. Am. Philos. Soc.* **93**, 521 (1949); *Proc. Natl. Acad. Sci. U.S.A.* **38**, 449 (1952).
3. J. C. Pati and A. Salam, *Phys. Rev. Lett.* **31**, 661 (1973); *Phys. Rev. D* **8**, 1240 (1973); *ibid.* **10**, 275 (1974); H. Georgi and S. L. Glashow, *Phys. Rev. Lett.* **32**, 438 (1974); H. Georgi, H. R. Quinn, S. Weinberg, *ibid.* **33**, 451 (1974).
4. The possibility of baryon nonconservation was discussed by G. Feinberg and M. Goldhaber [*Proc. Natl. Acad. Sci. U.S.A.* **45**, 1301 (1959)].
5. We are excluding the well-known possibility of beta-decay of free neutrons and certain bound nucleons.
6. F. Reines and M. F. Crouch, *Phys. Rev. Lett.* **32**, 493 (1974).
7. Abbreviations: p, proton; e^+, positron; γ, gamma; n, neutron; and ν, neutrino.
8. Note that the last-mentioned mode implies simultaneous violation of baryon conservation and electric charge conservation. The experimenter would be wise not to exclude such processes from consideration a priori.
9. G. N. Flerov, D. S. Klochkov, V. S. Skobkin, V. V. Terent'ev, *Sov. Phys. Dokl.* **3**, 79 (1958).
10. F. E. Dix, thesis, Case Western Reserve University (1970).
11. S. P. Rosen, *Phys. Rev. Lett.* **34**, 774 (1975).
12. T. Kirsten and H. W. Müller, *Earth Planet. Sci. Lett.* **6**, 271 (1969).
13. E. W. Hennecke, O. K. Manuel, D. D. Sabu, *Phys. Rev. C* **11**, 1378 (1975).
14. We neglect alpha-particle emission, which would be highly suppressed by Coulomb barrier effects.
15. A. Calboreanu and S. Mancas, *Nucl. Phys. A* **266**, 72 (1976).
16. G. Jacob and Th. A. J. Maris, *Rev. Mod. Phys.* **45**, 6 (1973).
17. There is some uncertainty in the literature as to the precise value of this lifetime. To be conservative, we have chosen the most recently published value, which also happens to be among the lowest. For a relatively recent summary of the literature, see H. R. Hiddleston and C. P. Browne [*Nucl. Data Sheets* **13**, 133 (1974)].
18. J. Takagi, W. Hampel, T. Kirsten, *Earth Planet. Sci. Lett.* **24**, 141 (1974).
19. The nucleon lifetime limit τ is obtained as
$$\tau = \tau_{\beta\beta} \times 52 \times \frac{^{130}Xe^c}{^{129}Xe^c}$$
where $^{130}Xe^c$ is the net ^{130}Xe produced by double beta-decay and $^{129}Xe^c$ is given by $^{129}Xe^c = {}^{129}Xe^{net} - 1.6\ ({}^{131}Xe^{net})$, using values given in Table 1 and $\tau_{\beta\beta} = 1.4 \times 10^{21}$ years. It is assumed that there are 52 nucleons per nucleus available for decay.
20. R. I. Steinberg and W. Maenhaut, *Lett. Nuovo Cimento* **15**, 93 (1976).
21. R. I. Steinberg, J. C. Evans, Jr., E. L. Fireman, paper presented at the International Conference on Neutrino Physics, Elbrus, Soviet Union, June 1977.
22. We thank M. Goldhaber for helpful discussions on this subject and R. Davis, Jr., for providing encouragement as well as pointing out several key references. Research was carried out at Brookhaven National Laboratory under contract with the Energy Research and Development Administration and supported by its Division of Physical Research. Research carried out at the University of Pennsylvania was supported in part by the Energy Research and Development Administration and by the Research Corporation.
* Present address: Physical Sciences Department, Battelle-Northwest, Richland, Wash. 99352.

17 February 1977; revised 31 May 1977

Microwave Spectroscopic Imagery of the Earth

Abstract. *The microwave spectrometer on the Nimbus 6 satellite has produced the first microwave spectral images of the earth. It has yielded global maps of (i) atmospheric temperature profiles, (ii) the distributions of water vapor and liquid water over ocean, and (iii) the coverage and type of ice and snow. The method has potential for operational synoptic monitoring.*

The use of passive microwave techniques to monitor geophysical phenomena began with radio astronomical observations of the solar system and the terrestrial atmosphere and surface (*1, 2*). The general principles of passive microwave sensing have been reviewed by Staelin (*3*).

The first spacecraft instrument to combine microwave spectrometry with imaging is the scanning microwave spectrometer (SCAMS). It was launched on 12 June 1975 together with companion sensors operating at visible, infrared, and a single microwave frequency. Most of these experimental sensors, including SCAMS, were designed as precursors to systems for the operational monitoring of the earth.

One of the primary objectives of the SCAMS experiment was to carry out global observations at 12-hour intervals of three geophysical parameters: atmospheric temperature profiles between altitudes of 0 and 20 km, the distributions of precipitable atmospheric water vapor and liquid water over ocean, and the microwave spectral emission of land, snow, and ice. A second goal was to determine the accuracy with which such parameters can be measured. The third aim consisted of a scientific and engineering evaluation of SCAMS and of similar microwave-sensing systems as one element in a global system for data collection.

The SCAMS system was fabricated at the Jet Propulsion Laboratory of the California Institute of Technology. It is

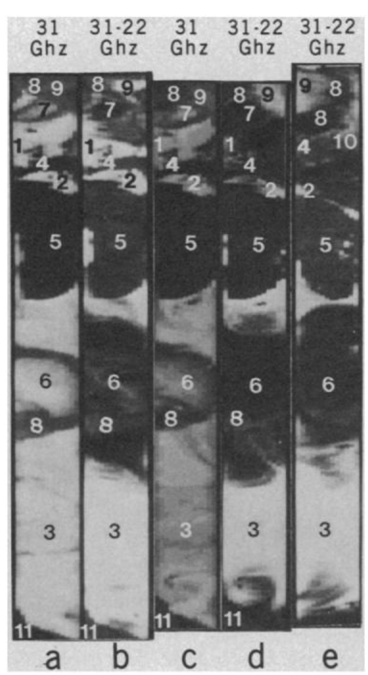

Fig. 1. Brightness temperature images for three orbits: (a and b) orbit 431, 14 July 1975; (c and d) orbit 2375, 6 December 1975; and (e) orbit 2449, 11 December 1975. In each image darker elements correspond to relatively higher brightness temperatures at 31.65 Ghz. Europe and Africa are seen in the top half of each image and Antarctica is in the center; however, in (e) the pass descended westward over Africa so as to include more of Asia than in (a) through (d). The images are compressed at the sides because the 13 view angles are equally spaced horizontally. Areas: 1, North Atlantic; 2, Mediterranean; 3, Pacific; 4, Europe; 5, Africa; 6, Antarctica; 7, Greenland; 8, newer sea ice; 9, older sea ice; 10, Siberian snow; and 11, North America.

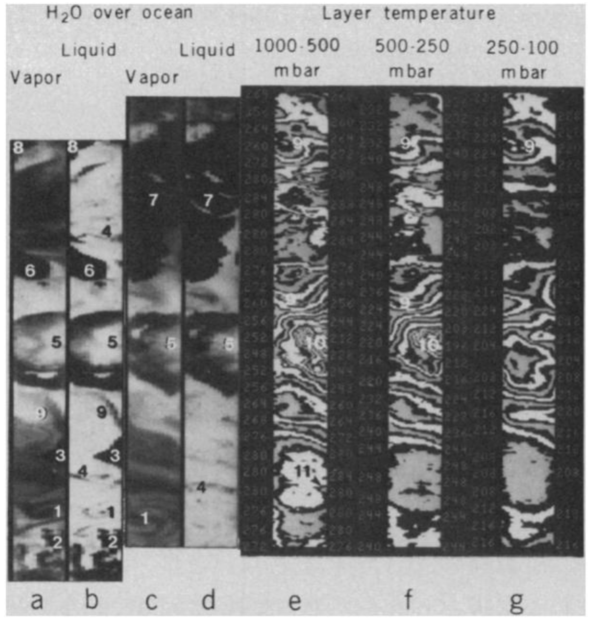

Fig. 2. Retrievals of atmospheric parameters for two orbits: (a and b) orbit 1050, 29 August 1975, and (c through g) orbit 1044, 29 August 1975. In (a) through (d) atmospheric water appears as dark streaks over the oceans; over land or ice the images have no significance. In (a) and (b) are seen part of the Pacific Ocean around Australia in the top half, and the Atlantic Ocean with the tip of Brazil protruding in the lower half. Images (c) through (g) show Asia, Africa, and part of the Indian Ocean in the top half and the mid-Pacific in the lower half. Antarctica is in the center of each image. Each of the bands in (e) through (g) has a width of 2 K; the numbers at the margins are the temperatures (in kelvins) at the lower boundary of the adjacent band. Areas: 1, cyclone; 2, Newfoundland; 3, Brazil, 4, intertropical convergence zone; 5, Antarctica; 6, Australia; 7, Saudi Arabia; 8, Kamchatka, U.S.S.R.; 9, frontal system; 10, land of high elevation; and 11, effects of clouds.

a microwave spectrometer having five independent superheterodyne radiometers centered on frequencies of 22.235, 31.65, 52.85, 53.85, and 55.45 Ghz (channels 1 through 5). This spectrometer is essentially an improved, scanning version of the Nimbus 5 microwave spectrometer (NEMS) (*2*). The polarization is linear for channels 1 through 4, with the electric vector parallel to the satellite velocity vector when SCAMS views nadir; it rotates an amount equal to the antenna scan angle. Channel 5 views the orthogonal linear polarization. The images that SCAMS produces cover a swath ~ 2500 km wide, which comprises 13 samples observed at equally spaced view angles; the resolution, which depends on the view angle, is ~ 150 to 300 km. A detailed description of the instrument is given in (*4*). The instrument functioned well after launch on 12 June 1975 and almost continuously from 2 July 1975 to 31 May May 1976, when the scan mechanism jammed.

The primary surface parameters determining microwave emission are surface temperature and surface emissivity, the product of which is the brightness temperature of the surface, T_B. The atmospheric opacity in polar regions normally contributes only a couple of degrees to the observed T_B values of channels 1 and 2 and can essentially be neglected in the analyses of surfaces. Five different surface regimes are evident in polar regions (*5*). These are (i) open ocean, (ii) snow-free land, (iii) sea ice, (iv) seasonal snow cover, and (v) permanent ice and snow over land, as in Antarctica and Greenland. Images of these regions obtained from SCAMS are shown in Fig. 1, where one July and two December orbits are presented. Each orbital image represents a pass from the North Pole to the South Pole and back.

Open ocean, the easiest regime to identify, is characterized by a very low 31.65-Ghz T_B, ~ 140 K, evident in Fig. 1, a and c, as light-colored regions. In both these images snow-free land, as in Africa and Europe, is nearly black, corresponding to a high T_B, near 280 K.

Sea ice is characterized by relatively high T_B values; such ice around Antarctica appears as a black band in Fig. 1, a and c. Sea ice also exhibits a range of differential T_B values, defined here as $T_B(31.65\ \mathrm{Ghz}) - T_B(22.235\ \mathrm{Ghz})$ and presented in Fig. 1, b, d, and e. Older sea ice tends to appear cooler (lighter in Fig. 1) at 31.65 Ghz than at 22.235 Ghz; for example, the north polar ice cap, which appears dark in Fig. 1, a and c (areas 8 and 9), is differentiated into light and dark regions in Fig. 1, b, d, and e. The newer north polar ice (area 8) is particularly evident in Fig. 1e as the dark band running between the older ice pack to the north and the snow-covered land to the south. Such an effect of ice age on microwave emission has been observed by others (*6*).

Seasonal snow over land is most evident in Fig. 1e as the whiter zones of northern Siberia and as bands in eastern Europe and middle Asia, for example, north of the Black Sea. Since observations at a single frequency, such as 31.65 Ghz, are ambiguous with respect to snow cover, these two-frequency differential T_B maps may provide a unique way to remotely map snow cover and perhaps snow depth. A comparison of the results of theoretical (*7*) and experimental (*5*) studies suggests that this snow signature arises from the internal scattering of microwave radiation by inhomogeneities in the snow, the shorter wavelength scattering more than the longer wavelength. Unless the snow is deeper than the nominal penetration depth of microwaves, the soil beneath the snow will also contribute to the emitted signal, thus diminishing the snow signature. This penetration depth appears to be on the order of 1 m for snow in the antarctic highlands, as deduced from NEMS data (*5*).

Permanent snow and ice over land is most evident in Greenland and Antarctica. The signature is characterized (Fig. 1, a and c) by very low 31.65-Ghz T_B values, near 140 to 160 K, below those for most other snow or ice. The differential T_B values (Fig. 1, b and d) vary roughly from +10 to −20 K, with the shorter wavelength T_B generally being warmer when the snow surface is warmer than the subsurface. The most surprising result from SCAMS was the discovery of large geographic zones with unique spectral signatures. Antarctica (Fig. 1b) particularly illustrates this phenomenon. These microwave spectral features appear to change in amplitude more than in shape, and to change predominantly on a seasonal basis. For example, the wintertime antarctic fine structure (Fig. 1b) largely disappeared in summer (Fig. 1d). Such slow seasonal variations are consistent with the idea that spectral features arise predominantly from levels within a few feet of the surface. Thus such microwave spectral observations appear to provide a unique new tool for studying the climatology of snow structure in these nearly inaccessible regions.

The T_B of snow-free land is generally dominated by a combination of climatological variations in surface temperature and localized variations in the soil moisture content (*8*). Neither of these effects is clearly evident in Fig. 1, although they are in the numerical data. Figure 1, b, d, and e, however, does show interesting variations in the differential T_B values over Africa. The origin of these spectral features has not been completely determined.

The 22.235- and 31.65-Ghz channels respond over ocean primarily to atmospheric water vapor and clouds. At these frequencies, both water vapor and liquid water appear in emission over ocean, which has an emissivity near 0.5. The 22.235-Ghz channel is approximately 2.5 times more sensitive to water vapor than the 31.65-Ghz channel, whereas it is only half as sensitive to liquid water. Thus, if observations are made at these two frequencies, it is possible to infer total water vapor and liquid water abundances separately (*9*). The root-mean-square (r.m.s.) theoretical accuracies (*9*) are ~ 0.2 g per square centimeter of water vapor, compared to experimental r.m.s. discrepancies with radiosonde records of ~ 0.4 g cm^{-2}; the total range of water vapor measurable is ~ 0 to 6 g cm^{-2}. The estimates of liquid water have theoretical r.m.s. errors of ~ 0.01 g cm^{-2} (*9*), which is a small fraction of the maximum values inferred, 0.25 g cm^{-2}. These peak observed values are lower than those that can occur within single convection cells because the nominal 150-km resolution of SCAMS averages such wet cells with their drier surroundings. We know of no conventional measurements of liquid water for easy comparison on this size scale.

Figure 2, a through d, presents estimates of water vapor and liquid water over ocean. Over land or ice these images have no specific significance. The humidity patterns illustrated here differ significantly from those now obtained by other remote-sensing techniques such as infrared spectroscopy, because these microwave soundings respond strongly to the humidity present in the layer between 0 and 2 km. This bottom layer is otherwise very difficult to sound accurately, although it contains most of the water vapor. The most significant features in these humidity distributions are the cyclonic storm south of Newfoundland, near the bottom of Fig. 2a, and the striations in the equatorial humidity distribution shown near the bottom of Fig. 2c. In some cases the striations appear to be indicative of vertical atmospheric motions. The intertropical convergence zone (ITCZ) is evident in Fig. 2, b and d, near the equator. Other long thin bands of large liquid water concentrations, which are predominantly precipitation, are also evident in Fig. 2.

Representative climatological averages of these water vapor and liquid water estimates appear on the cover. Both images represent averages of data obtained between 15 August and 29 August 1975; the upper image portrays the water vapor distribution over ocean, and the lower image maps liquid water. The liquid water images are spuriously increased near Antarctica, an effect probably due to very rough seas and an insufficient number of microwave channels.

The oxygen absorption band at a wavelength from 4 to 6 mm results in atmospheric attentuation ranging from ~ 0 to 200 db. Therefore, the upwelling microwave thermal emission can originate from altitudes anywhere between the terrestrial surface and the mesosphere, depending on the wavelength. Channels 3, 4, and 5 of SCAMS measure the average temperatures of layers ~ 10 km thick centered near altitudes of 2, 6, and 13 km, respectively. The original suggestion to use the microwave oxygen spectrum this way was made by Meeks and Lilley (*10*), and results from the NEMS experiment (*11*) confirmed the practicality of this idea.

The retrieved atmospheric temperature profile is presented here as the average temperature, weighted by the logarithm of pressure, over three atmospheric layers, that is, those lying in the intervals between 1000 and 500 mbar, 500 and 250 mbar, and 250 and 100 mbar. Contour maps of these variables are shown in Fig. 2, e through g, corresponding to Fig. 2, c and d. The most significant features in these maps are the strong thermal wave over Asia and a smaller wave below Antarctica. The atmospheric circulation pattern suggested by the spiral features of water vapor (Fig. 2c) is also evident in the contours between 250 and 100 mbar (Fig. 2g). The effects of land of high elevation are not compensated in these images; hence the antarctic highlands, which penetrate the atmospheric layers being sounded, introduce considerable error in the levels from 1000 to 500 mbar and from 500 to 250 mbar, as shown. The effects of precipitation on these temperature retrievals are just barely evident in Fig. 2e over the ITCZ, where there is a slight spatial perturbation in the retrieved temperature map. We have largely eliminated the effects of land-sea boundaries by utilizing the 22.235- and 31.65-Ghz data, and more sophisticated data-reduction algorithms could offer still further improvement. The predicted r.m.s. errors for these layer average temperatures are approximately 1.8 K, and comparisons with National Meteorological Center 0^h and 12^h analyses, interpolated in time and space to SCAMS coordinates, have yielded essentially identical results, that is, r.m.s. errors of 1.7 K. This analysis was based on 2000 soundings over the entire Northern Hemisphere for sites with surface elevations below 1 km.

The geophysical maps (Figs. 1 and 2) demonstrate some of the unique capabilities of passive microwave imaging spectrometers in planetary orbits. The most important capabilities demonstrated by SCAMS are the following: (i) the insensitivity of the microwave soundings to most clouds; (ii) the fact that the instrument can be used to penetrate and map subsurface structural and thermal parameters for media such as dry ice and snow which are semitransparent at these wavelengths; and (iii) the fact that the instrument can be used to map atmospheric temperature profiles and distributions of atmospheric constituents having microwave spectral signatures, such as water vapor and liquid water. Improvements in instrument sensitivity, frequency coverage, and spatial resolution are under way, and the results reported here are merely suggestive of the potential usefulness of imaging microwave spectrometers.

D. H. STAELIN
P. W. ROSENKRANZ
Research Laboratory of Electronics, Massachusetts Institute of Technology, Cambridge 02139

F. T. BARATH
E. J. JOHNSTON
J. W. WATERS
Jet Propulsion Laboratory, California Institute of Technology, Pasadena 91103

References and Notes

1. F. T. Barath, A. H. Barrett, J. Copeland, D. E. Jones, A. E. Lilley, *Astron. J.* **69**, 49 (1964); A. E. Basharinov, A. S. Gurvich, S. T. Yegorov, *Dokl. Akad. Nauk SSSR* **188**, 1273 (1969); T. T. Wilheit, in *Nimbus 5 User's Guide*, R. R. Sabatini, Ed. (NASA Goddard Space Flight Center, Greenbelt, Md., 1972), p. 59.
2. D. H. Staelin, A. H. Barrett, J. W. Waters, F. T. Barath, E. J. Johnston, P. W. Rosenkranz, N. E. Gaut, W. B. Lenoir, *Science* **182**, 1339 (1973).
3. D. H. Staelin, *Proc. IEEE* **57**, 427 (1969).
4. ———, A. H. Barrett, P. W. Rosenkranz, F. T. Barath, E. J. Johnston, J. W. Waters, A. Wouters, W. B. Lenoir, in *Nimbus 6 User's Guide*, J. E. Sissala, Ed. (NASA Goddard Space Flight Center, Greenbelt, Md., 1976), p. 59.
5. K. F. Kunzi, A. D. Fisher, D. H. Staelin, J. W. Waters, *J. Geophys. Res.* **81**, 4965 (1976).
6. T. T. Wilheit, W. Nordberg, J. C. Blinn III, W. J. Campbell, A. T. Edgerton, *Remote Sensing Environ.* **2**, 129 (1972); P. Gloersen, T. T. Wilheit, T. C. Chang, W. Nordberg, W. J. Campbell, *Bull. Am. Meteorol. Soc.* **55**, 1442 (1974).
7. L. Tsang and J. A. Kong, *Radio Sci.* **11**, 599 (1976).
8. T. Schmugge, P. Gloersen, T. T. Wilheit, F. Geiger, *J. Geophys. Res.* **79**, 317 (1974).
9. P. W. Rosenkranz, F. T. Barath, J. C. Blinn III, E. J. Johnston, W. B. Lenoir, D. H. Staelin, J. W. Waters, *ibid.* **77**, 5833 (1972); D. H. Staelin, K. F. Kunzi, R. L. Pettyjohn, R. K. L. Poon, R. W. Wilcox, J. W. Waters, *J. Appl. Meteorol.* **15**, 1204 (1976), N. Grody, *IEEE Trans. Antennas Propag.* **AP-24**, 155 (1976).
10. M. L. Meeks and A. E. Lilley, *J. Geophys. Res.* **68**, 1683 (1963).
11. J. W. Waters, K. F. Kunzi, R. L. Pettyjohn, R. K. L. Poon, D. H. Staelin, *J. Atmos. Sci.* **32**, 1953 (1975); D. H. Staelin, A. L. Cassel, K. F. Kunzi, R. L. Pettyjohn, R. K. L. Poon, P. W. Rosenkranz, *ibid.*, p. 1970.
12. We thank A. H. Barrett, N. E. Gaut, W. B. Lenoir, W. Nordberg, and N. Phillips for their help in the formative stages of the experiment, and K. F. Kunzi, W. L. Ledsham, R. L. Pettyjohn, and A. Wouters for their assistance in implementing it. A. D. Fisher and D. E. Troxel collaborated in preparing the global images on the cover. The program is supported by NASA contract NAS5-21980.

10 August 1976; revised 13 April 1977